Pressure, temperature and three-component-velocity fields by filtered Rayleigh scattering velocimetry

ULRICH DOLL[1,*], GUIDO STOCKHAUSEN[2], AND CHRISTIAN WILLERT[2]

[1] Paul Scherrer Institute, Laboratory of Thermal Processes and Combustion, CH-5232 Villigen PSI
[2] German Aerospace Center (DLR), Institute of Propulsion Technology, Measurement Technology, Linder Hoehe, D-51147 Cologne
[*] Corresponding author: ulrich.doll@psi.ch

Compiled August 18, 2017

The filtered Rayleigh scattering (FRS) technique, extended by the method of frequency scanning (FSM-FRS), is a powerful tool to characterize thermodynamic as well as aerodynamic properties of technical flows. In this letter, we report on the first application of an FRS velocimeter, which is capable of acquiring time-averaged planar pressure, temperature and three-component velocity distributions simultaneously. The method is validated by characterizing the near-field as well as the far-field of a turbulent jet.

OCIS codes: *120.0120, 120.5820, 120.6780, 120.7250, 120.5475, 290.5870*

http://dx.doi.org/10.1364/OL.42.003773

The knowledge of thermodynamic as well as aerodynamic properties of gaseous flows is of great interest in a wide variety of technical applications. While most laser-optical measurement methods are limited to measure only a single quantity, the filtered Rayleigh scattering (FRS) technique [1], extended by the method of frequency scanning (FSM-FRS), is capable to simultaneously provide time-averaged planar information on pressure, temperature and flow velocity [2, 3]. To this date, the method was used to measure one single scalar frequency-shift, which could then be interpreted as flow velocity from some prior knowledge concerning the structure of the flow field [3–5]. In this letter, we report on an FSM-FRS system, which, in addition to time-averaged pressure and temperature fields, delivers three-component (3C) velocity distributions. The method will be tested by characterizing the near-field as well as the far-field of a turbulent jet in air.

Velocity measurements by FRS are based on the optical Doppler frequency-shift

$$\Delta\nu = \frac{\nu_0}{c}(\mathbf{o} - \mathbf{l}) \cdot \mathbf{v}\,, \qquad (1)$$

with ν_0 as excitation frequency, c as speed of light, $\mathbf{o}$ as vector pointing from the interrogation volume to the observer, $\mathbf{l}$ as vector in light sheet direction and $\mathbf{v}$ as 3C flow velocity. In contrast to established planar 3C velocimetry methods such as stereoscopic particle image velocimetry (SPIV) [6] or Doppler global velocimetry (DGV) [7], which both infer their measured signal by adding tracer particles to the flow, FRS solely relies on molecular scattering. In order to use the technique to acquire 3C velocity distributions, similar to DGV, either light sheet orientation or observer position have to be varied [7]. The FSM-FRS system presented herein is based on the latter principle. By means of a multiple-branch image fiber bundle, the interrogation area is observed from three directions. While temperature and pressure for all observers are the same, according to equation 1, the varying scattering geometry leads to differing Doppler frequency-shifts for each single branch, from which the 3C velocity field can then be reconstructed [8, 9].

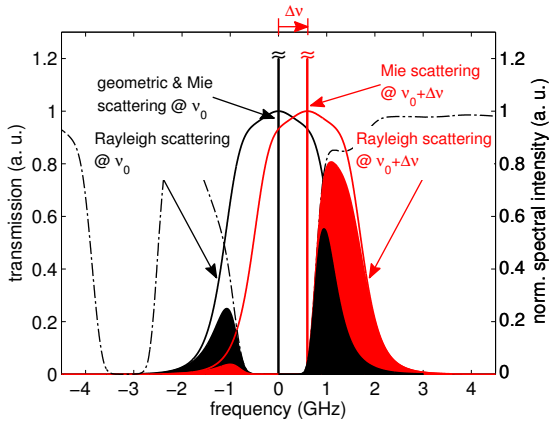

Fig. 1. Spectrally broadened Rayleigh scattering at excitation frequency ν_0 (black curve) is frequency-shifted by an amount of $\Delta\nu$ due to flow velocity (red curve). While geometric and Mie scattering is removed by the molecular filter (dashed-dotted curve), portions of spectrally broadened Rayleigh scattering reach the detector.

Figure 1 shows the FRS technique's working principle and its extension to velocimetry. By means of molecular absorption, strong narrow-band elastic scattering components such as geometric scattering from surfaces/windows or Mie scattering from large particles are cancelled out, while part of the Rayleigh scattering's spectral distribution is transmitted. The spectral shape of laser-induced Rayleigh scattering is a result of broadening mechanisms associated with molecular motion. When

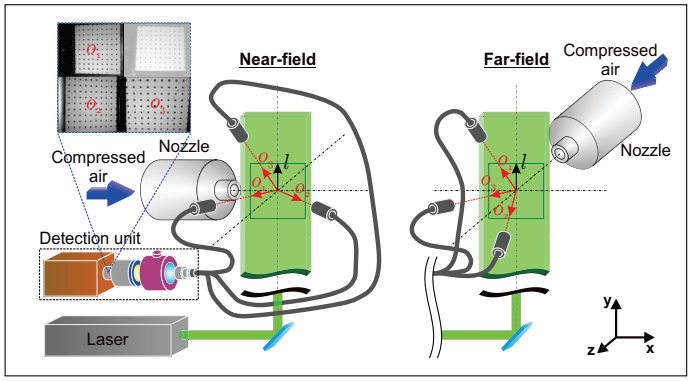

Fig. 2. Principle setup and optical arrangement for near-field (left) and far-field (right) characterization: The laser beam is formed into a light sheet propagating along **l**. Scattered light is collected along $\mathbf{o}_1$, $\mathbf{o}_2$, $\mathbf{o}_3$ and enters the detection unit, where it is transmitted through the iodine filter (pink) as well as a bandpass filter (blue). The signal is imaged onto the detector using a pair of objective lenses into retro-arrangement (gray). The resulting image is divided in quadrants with respect to the corresponding branch of the image fiber bundle (upper left corner).

laser light is scattered from an ensemble of gas molecules, the height of the resulting spectrum is related to density (or pressure, when the ideal gas law is assumed), width and shape are associated with pressure and temperature. While thermodynamic quantities have influence on the Rayleigh scattering's spectral lineshape, according to equation 1, the entire scattering spectrum is frequency-shifted from its excitation wavelength along the molecular filter's transmission curve by an amount proportional to flow velocity [10, 11]. By this, the Doppler frequency-shift is transformed into an intensity change, which can then be detected by a sensitive camera. The concept of FRS velocimetry is analogue to the DGV technique's working principle [7], despite that the spectral response of particle scattering is much narrower than molecular Rayleigh scattering and thus potentially better suited to achieve high velocity accuracies.

Experimental setups for both near-field as well as far-field characterization of the turbulent jet flow are depicted in figure 2. The jet flow experiment is based on a subcritical nozzle with an exit diameter of 20 mm and a contraction ratio of 9. To reduce inlet fluctuations, compressed air is passed through a settling chamber and an array of honeycombs before expansion. Operating conditions are set by measuring total pressure and temperature inside the settling chamber. With ambient pressure known, the main velocity component as well as the temperature inside the jet's potential core can be calculated from isentropic relations. For near-field measurements, the jet propagates along the x-axis while in case of far-field characterization, the nozzle is placed at 221 mm distance from the interrogation area with the main velocity component pointing in z-direction.

The FSM-FRS system is based on a Coherent Verdi V5 continuous wave laser, emitting single-frequency light at 532 nm with an output power of up to 5 W and a bandwidth < 5 MHz. The laser's frequency can be modified by heating or cooling an intra-cavity etalon as well as by issuing control voltages on two piezoelectric elements and thus altering the resonator's length. The frequency is monitored and actively controlled by a High Finesse WSU 10 wavelength meter, which has an absolute accuracy of 10 MHz and enables, by issuing a control voltage on one of the piezos, a relative stability of the laser's output frequency below 2 MHz of the setpoint. A second control loop accounts for thermal effects in the laser's resonator and ensures long-term frequency stability. As FRS signal intensities depend on the incident laser energy, a photodiode continuously records the relative intensity variations throughout the experiments.

The scattered light is collected by a multiple-branch image fiber bundle [8, 9]. C-mount lenses image the light onto the respective branches of image fiber bundles, which have an active area of 6 x 5 mm^2 consisting of 600 x 500 fiber elements. An image of the distal end of the image fiber bundle is depicted in the upper left corner of figure 2. The frame is divided into four quadrants, each containing the field of view of a single observer position. As indicated by the transparent box, only quadrants 1, 2 and 3 were used in the experiments. The light emitted by the image bundles next enters the transfer optics, which is composed of two additional lenses in retro arrangement. Between the two lenses, a molecular iodine filter cell as well as a bandpass filter (Barr, FWHM 1 nm) are placed. The iodine filter consists of an evacuated glass cylinder, 50 mm in outer diameter and length, filled with a fixed amount of crystalline iodine. The cylinder is mounted into a temperature controlled housing. Above a certain saturation temperature of 70°C, all crystalline iodine is evaporated, leading to homogenous absorption throughout the cell body as well as preventing jumps in the filter's transmission by spontaneous evaporation of iodine. Light exiting the filter array is accumulated by a Hamamatsu C9100-13 EM-CCD camera.

The basic idea of the FSM-FRS technique is to scan the laser's output frequency along the molecular filter's transmission curve. According to [2, 3], total FSM-FRS signal intensities per sensor element ij at frequency step k can be written as

$$S_{ijkl}(\nu_{0,k}, p_{ij}, T_{ij}, \Delta\nu_{ijl}, \Theta_{ijl}) = I_0 n_{ij} R_{ijl} \int_{-\infty}^{\infty} r_{ijl}(\nu - \nu_{0,k}, p_{ij}, T_{ij}, \Delta\nu_{ijl}, \Theta_{ijl}) \tau(\nu) \mathrm{d}\nu \,, \quad (2)$$

where I_0 is the incident laser intensity and R the optical setup's efficiency. The integral describes the convolution between the Rayleigh scattering's spectral lineshape r, which depends on the excitation frequency ν_0, pressure p, temperature T, scattering angle Θ (which is $\arccos(\mathbf{o} \cdot \mathbf{l})$) and the molecular filter's transmission curve τ, which incorporates the Doppler frequency-shift $\Delta\nu$. The subscript l is added to the formulation in order to denote the varying observer positions with regard to the multiple branches of the wound image bundle.

FSM-FRS measurement accuracy strongly relies on an accurate modelling of Rayleigh scattering's spectral distribution. In [12] it was shown, that the standard lineshape model by Tenti *et al* [13] introduces a bias between measured results and analytical solution to a reference experiment. Thus, a calibrated analytical model function was proposed, which significantly reduced these deviations. In the following, the data evaluation procedure is based on the calibrated analytical lineshape model.

According to equation 2, the scattering angle varies with each element of the camera sensor as well as observer position. Θ has influence on the Rayleigh scattering's spectral lineshape and is thus considered likely of introducing additional measurement uncertainties. In order to calibrate observer positions, methods given in [14] are applied to the dot-pattern image depicted in figure 2, yielding point correspondences to map the

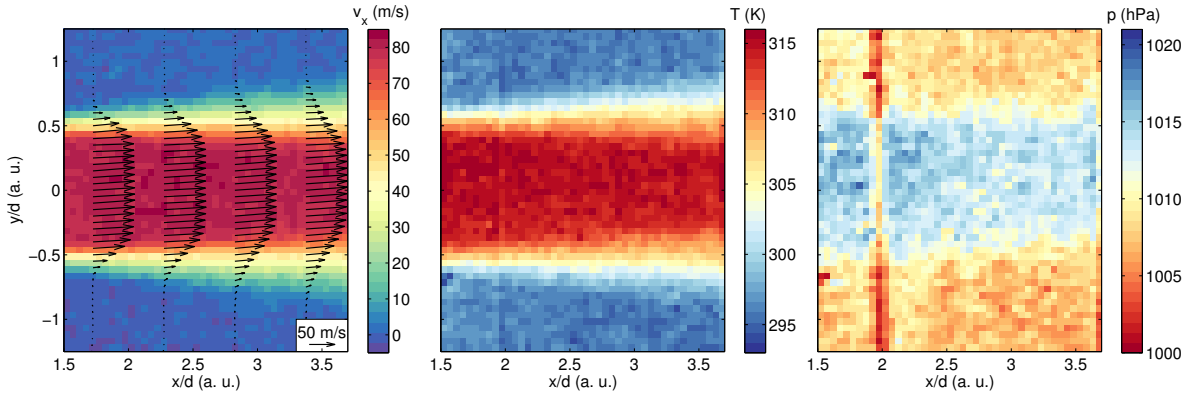

Fig. 3. Near-field results: Main velocity component v_x (*left*), temperature (*middle*) and pressure fields (*right*). Velocity vectors indicate v_x and v_y velocity components.

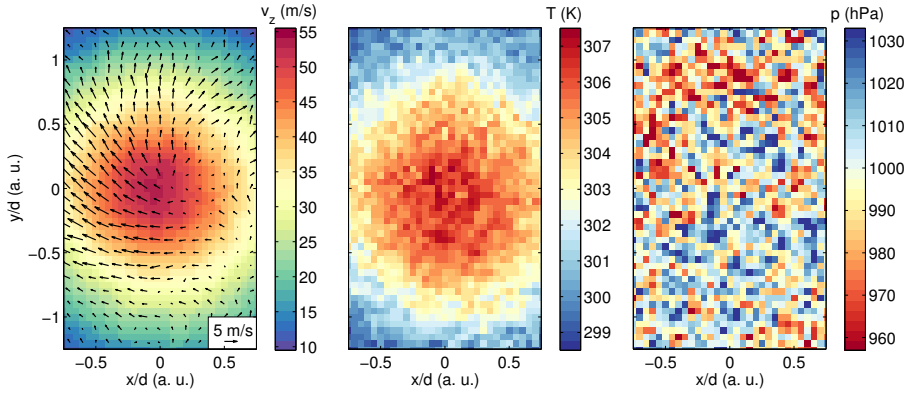

Fig. 4. Far-field results: Main velocity component v_z (*left*), temperature (*middle*) and pressure fields (*right*). Velocity vectors indicate v_x and v_y velocity components.

Table 1. Near-field results compared to analytical solution

	analyt. sol.	FRS
p (hPa)	1011 ± 1	$1013 \pm 5(0.7)$
T (K)	314 ± 2	$315 \pm 1.2(0.5)$
v_x (m/s)	82 ± 1	$82 \pm 1.4(0.8)$

three camera views onto each other as well as coordinates of a vector pointing from the user defined origin in the object plane towards an idealized lens (pinhole) for each of the three detection branches. With the spatial resolution known, an **o**-vector and thus scattering angle can be assigned to each camera pixel.

The optical efficiency parameter R at each sensor element is derived from a reference frequency scan with pressure, temperature known and zero flow velocity [3]. Regarding the three observer positions with varying optical properties, this has to be performed for all camera views. In order to use optical efficiencies obtained from a reference dataset to evaluate experimental data gathered under operating conditions, these may stay unchanged until all experiments are concluded. While this procedure delivers good results in case of the near-field characterization, the far-field data suffers from changing R-values due to a minor shift of the imaged frame on the camera sensor, which was probably caused by an unstable camera mount. Nevertheless, the far-field data can still be evaluated by means of the normalization procedure presented in [12]: In dividing each signal intensity S_{ijkl} by it's ensemble average over all frequencies $\langle S_{ijl} \rangle$, the optical efficiency R is cancelled from the model equation. While the procedure is beneficial in this respect, pressure sensitivity is reduced by more than an order of magnitude [12].

Results for velocity, temperature and pressure of the near-field characterization are depicted in figure 3. The field of view starts 1.5 nozzle diameters downstream from the nozzle exit and extends about 2.2 diameters in axial direction. Maps of axial velocity and temperature show a typical near-field topology, with constant values inside the jet's potential core, strong gradients in the growing shear layer and ambient conditions in the almost undisturbed outer region. The weak upward orientation of velocity vectors is related to a slight misalignment of the nozzle axis with respect to measurement plane. As the flow expands into ambient, constant pressure is expected throughout the imaged area. Nevertheless, FRS results show a slight increase of static pressure in the jet's core region. The deviation is in accordance with findings in [12] and are probably related to systematic effects introduced by the calibrated analytical lineshape model. The artifact visible at $x/d = 2$ in pressure as well as, to a lesser extend, in temperature results, can be associated with dust particles contaminating the light sheet optics after the reference run. This leads to a slight decrease of the optical efficiency parameter R of equation 2 for data gathered under op-

erating conditions, which finally is interpreted as lower density and thus lower pressure by the data evaluation algorithm.

Table 1 shows a comparison of near-field FRS results, spatially averaged over the region of constant axial velocity, to ambient pressure, measured with a calibrated hand-held device and temperature as well as main velocity component inside the potential core, which are calculated from isentropic relations. Uncertainties to the jet experiment's analytical solution are mainly introduced by variations of inlet pressure and temperature due to fluctuations in the air supply. Given FRS uncertainties express the standard deviation of the spatial average inside the potential core. In addition, uncertainty values in parentheses are determined by the simplified Monte-Carlo method introduced in [12].

Spatial averages of near-field FRS pressure, temperature and velocity results are in good agreement to the analytical solution. Concerning uncertainties, the spatial variation of the measurands is significantly higher compared to values estimated from the Monte-Carlo analysis. A similar effect was observed in [15], where spatial temperature variations could be related to the fiber structure of the image fiber bundle.

In figure 4, maps of far-field velocity and temperature exhibit the typical Gaussian shape of a fully developed turbulent jet flow. As well as in figure 3, non-zero transverse velocities are caused by a slight misalignment of jet axis and light sheet. Above it was indicated that the modified model equation results in lower pressure sensitivity. This is expressed through a higher spatial variation of ± 19 hPa of far-field pressures compared to near-field results.

In figure 5, profiles of velocity and temperature obtained with FRS are compared to experimental literature data. As the flow in the far-field is self-similar, experimental results of differing nozzle geometries and inlet conditions can be compared [16]. Therefore, $v_{\mathbf{z}}$ is normalized to the centerline velocity $v_{\mathbf{z,c}}$ and plotted against $|y/y_{\mathbf{0.5v}}|$. $y_{\mathbf{0.5v}}$ is the radial distance from the nozzle axis, where the normalized main velocity is one half of the centerline value. In order to compare temperatures, the difference between experimental results T and ambient temperature T_∞ is normalized to the difference of centerline temperature $T_{\mathbf{c}}$ and T_∞. The quotient is plotted against $|y/y_{\mathbf{0.5T}}|$, where $y_{\mathbf{0.5T}}$ represents the coordinate where the normalized temperature is one half of the centerline value.

FRS velocities and temperatures as well as literature results are in good agreement within their respective spreading. Half-width coordinates $y_{\mathbf{0.5v}}$ and $y_{\mathbf{0.5T}}$ of velocity and temperature fields can be interpreted as lateral growth of the jet flow in streamwise direction [17]. Comparing both half-widths, the growth of the temperature distribution exceeds the velocity field's extend by 22 %. Discrepancies in normalized velocities for $|y/y_{\mathbf{0.5v}}| > 1.35$ are probably related to the distance of the measurement plane of only 10 nozzle diameters, which may be too short to reach complete self-similarity.

In this letter, an FRS velocimeter is designed and successfully brought into use. The method is applied to characterize thermodynamic as well as aerodynamic properties of a turbulent jet flow. Spatially averaged near-field pressure, temperature and velocity results show very good agreement compared to analytically calculated reference values. Far-field velocity and temperature profiles exhibit a Gaussian topology, which is typical to fully developed turbulent jet flows. Normalized velocities and temperatures in the self-similar region are in good agreement to literature data. It is shown, that FRS velocimetry in combination with the method of frequency scanning, has

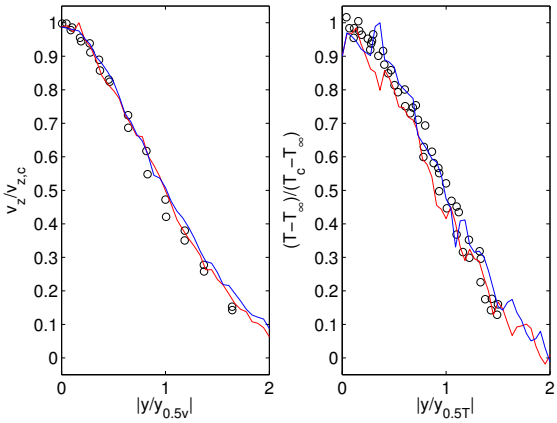

Fig. 5. Upper (red) and lower (blue) branches of non-dimensional far-field velocity (*left*) and temperature (*right*) profiles compared to experimental literature data [18, 19].

the capability to simultaneously provide pressure, temperature and 3C velocity maps with absolute uncertainties below 5 hPa, 1.2 K as well as 1.4 m/s respectively.

This work was supported and financed by the German Federal Ministry for Economic Affairs and Energy (BMWI), Grant No. 03ET07073E.

REFERENCES

1. R. B. Miles and W. R. Lempert, Applied Physics B: Lasers and Optics **51**, 1 (1990).
2. J. N. Forkey, "Development and Demonstration of Filtered Rayleigh Scattering: a Laser Based Flow Diagnostic for Planar Measurement of Velocity, Temperature and Pressure." Ph.D. thesis, Princeton University (1996).
3. U. Doll, G. Stockhausen, and C. Willert, Experiments in Fluids **55**, 1 (2014).
4. J. N. Forkey, W. R. Lempert, and R. B. Miles, Experiments in Fluids **24**, 151 (1998).
5. M. Boguszko and G. Elliott, Experiments in Fluids **38**, 33 (2005).
6. C. Willert, Measurement Science and Technology **8**, 1465 (1997).
7. J. F. Meyers and H. Komine, "Doppler global velocimetry-A new way to look at velocity," in "Laser Anemometry-Advances and Applications 1991," , vol. 1 (1991), vol. 1, pp. 289–296.
8. D. S. Nobes, H. D. Ford, and R. P. Tatam, Experiments in Fluids **36**, 3 (2004).
9. C. Willert, G. Stockhausen, M. Beversdorff, J. Klinner, C. Lempereur, P. Barricau, J. Quest, and U. Jansen, Experiments in Fluids **39**, 420 (2005).
10. H. Shimizu, S. A. Lee, and C. She, Appl. Opt. **22**, 1373 (1983).
11. A. Mielke, R. Seasholtz, K. Elam, and J. Panda, Experiments in Fluids **39**, 441 (2005).
12. U. Doll, E. Burow, G. Stockhausen, and C. Willert, Measurement Science and Technology **27**, 125204 (2016).
13. G. Tenti, C. Boley, and R. Desai, Canadian Journal of Physics **52**, 285 (1974).
14. C. Willert, Experiments in Fluids **41**, 135 (2006).
15. U. Doll, G. Stockhausen, J. Heinze, U. Meier, C. Hassa, and I. Bagchi, Journal of Engineering for Gas Turbines and Power **139**, 021507 (2016).
16. G. Lipari and P. K. Stansby, Flow, Turbulence and Combustion **87**, 79 (2011).
17. H. Schlichting and K. Gersten, *Grenzschicht-Theorie* (Springer-Verlag, 2006).
18. G. Xu and R. Antonia, Experiments in Fluids **33**, 677 (2002).
19. T.-H. Shih, J. L. Lumley, and J.-Y. Chen, AIAA Journal **28**, 610 (1990).

FULL REFERENCES

1. R. B. Miles and W. R. Lempert, "Two-dimensional measurement of density, velocity, and temperature in turbulent high-speed air flows by UV Rayleigh scattering," Applied Physics B: Lasers and Optics **51**, 1–7 (1990).
2. J. N. Forkey, "Development and Demonstration of Filtered Rayleigh Scattering: a Laser Based Flow Diagnostic for Planar Measurement of Velocity, Temperature and Pressure." Ph.D. thesis, Princeton University (1996).
3. U. Doll, G. Stockhausen, and C. Willert, "Endoscopic filtered Rayleigh scattering for the analysis of ducted gas flows," Experiments in Fluids **55**, 1–13 (2014).
4. J. N. Forkey, W. R. Lempert, and R. B. Miles, "Accuracy limits for planar measurements of flow field velocity, temperature and pressure using Filtered Rayleigh Scattering," Experiments in Fluids **24**, 151–162 (1998).
5. M. Boguszko and G. Elliott, "On the use of filtered Rayleigh scattering for measurements in compressible flows and thermal fields," Experiments in Fluids **38**, 33–49 (2005).
6. C. Willert, "Stereoscopic digital particle image velocimetry for application in wind tunnel flows," Measurement Science and Technology **8**, 1465–1479 (1997).
7. J. F. Meyers and H. Komine, "Doppler global velocimetry-A new way to look at velocity," in "Laser Anemometry-Advances and Applications 1991," , vol. 1 (1991), vol. 1, pp. 289–296.
8. D. S. Nobes, H. D. Ford, and R. P. Tatam, "Instantaneous, three-component planar Doppler velocimetry using imaging fibre bundles," Experiments in Fluids **36**, 3–10 (2004).
9. C. Willert, G. Stockhausen, M. Beversdorff, J. Klinner, C. Lempereur, P. Barricau, J. Quest, and U. Jansen, "Application of Doppler global velocimetry in cryogenic wind tunnels," Experiments in Fluids **39**, 420–430 (2005).
10. H. Shimizu, S. A. Lee, and C. She, "High spectral resolution lidar system with atomic blocking filters for measuring atmospheric parameters," Appl. Opt. **22**, 1373–1381 (1983).
11. A. Mielke, R. Seasholtz, K. Elam, and J. Panda, "Time-average measurement of velocity, density, temperature, and turbulence velocity fluctuations using rayleigh and mie scattering," Experiments in Fluids **39**, 441–454 (2005).
12. U. Doll, E. Burow, G. Stockhausen, and C. Willert, "Methods to improve pressure, temperature and velocity accuracies of filtered Rayleigh scattering measurements in gaseous flows," Measurement Science and Technology **27**, 125204 (2016).
13. G. Tenti, C. Boley, and R. Desai, "On the Kinetic Model Description of Rayleigh-Brillouin Scattering from Molecular Gases," Canadian Journal of Physics **52**, 285–290 (1974).
14. C. Willert, "Assessment of camera models for use in planar velocimetry calibration," Experiments in Fluids **41**, 135–143 (2006).
15. U. Doll, G. Stockhausen, J. Heinze, U. Meier, C. Hassa, and I. Bagchi, "Temperature measurements at the outlet of a lean burn single-sector combustor by laser optical methods," Journal of Engineering for Gas Turbines and Power **139**, 021507–021507–10 (2016).
16. G. Lipari and P. K. Stansby, "Review of experimental data on incompressible turbulent round jets," Flow, Turbulence and Combustion **87**, 79–114 (2011).
17. H. Schlichting and K. Gersten, *Grenzschicht-Theorie* (Springer-Verlag, 2006).
18. G. Xu and R. Antonia, "Effect of different initial conditions on a turbulent round free jet," Experiments in Fluids **33**, 677–683 (2002).
19. T.-H. Shih, J. L. Lumley, and J.-Y. Chen, "Second-order modeling of a passive scalar in a turbulent shear flow," AIAA Journal **28**, 610–617 (1990).